Nickel-zeolite composite catalysts with metal nanoparticles selectively encapsulated in the zeolite micropores

Deizi V. Peron[a,b], Vladimir L. Zholobenko[c], Melissa Rodrigues de la Rocha[a,b], Michèle Oberson de Souza[b], Liliana A. Feris[b], Nilson R. Marcilio[b], Vitaly V. Ordomsky[a] and Andrei Y. Khodakov[a]*

[a]*Univ. Lille, CNRS, Centrale Lille, ENSCL, Univ. Artois, UMR 8181 – UCCS – Unité de Catalyse et Chimie du Solide, F-59000 Lille, France*

[b]*Universidade Federal do Rio Grande do Sul - UFRGS, Porto Alegre, RS 90040-040, Brazil*

[c] *Keele University, School of Physical and Chemical Sciences, Staffordshire, ST5 5BG, United Kingdom*

**andrei.khodakov@univ-lille.fr* *(Corresponding author)*

Abstract

Metal zeolite composite catalysts have found numerous applications in adsorption, gas separation, petroleum refining and chemical industry. The key issue in the design of these catalysts is the localization of the metal within the zeolite structure. This paper focuses on a new approach to the synthesis of nickel-zeolite composite catalysts selectively containing metal nanoparticles inside the zeolite pores. In the catalysts prepared by conventional impregnation, metal particles from the external surface of the zeolites were selectively removed by extraction with bulky polymer molecules of poly-4-styrenesulfonic acid. The method is particularly suitable for the ZSM-5 zeolite with relatively narrow micropores. The nickel zeolite catalysts were tested in hydrogenation of toluene and 1,3,5 ï tri-isopropyl benzene (TIPB). The removal of nickel particles from the zeolite external surface leads to a considerable decrease in the hydrogenation rate of the bulky TIPB molecules, while toluene hydrogenation was affected to a much lesser extent and was almost proportional to the nickel content. The proposed methodology can be extended to other types of microporous catalysts.

Keywords: composites; encapsulation; zeolites; nickel; catalyst, micropores; shape-selectivity

Introduction

Zeolites, due to their acidic properties and microporosity, are important adsorbents, catalysts and catalytic supports for gas separation, petroleum refining [1-5] (e.g. catalytic cracking, hydrocracking, isomerization, alkylation, etc.) and chemical processes such as oxidation, fragrance synthesis, hydrogenation and for many other industrial reactions involving organic compounds. They are also considered for the synthesis of fine chemicals from biomass [6-8]. More recently, composite catalysts containing both metallic and zeolite active phases showed promising catalytic performance in syngas conversion to value-added products, such as direct single-step synthesis of liquid fuels from syngas [9,10] or synthesis of dimethyl ether [11].

Because of its reasonable cost, satisfactory catalytic performance and availability, nickel could be used in zeolite catalysts as an alternative to expensive noble metals. Nickel-zeolite catalysts have found their application in many important catalytic reactions: hydrogenation, isomerization, dehydrogenation, oxidation, oligomerisation, aromatization, hydrogen production, carbon nanotube preparation, NO_x reduction and hydrocracking [12-19].

Metal-zeolite catalysts often exhibit complex behaviour, because of their multicomponent composition and structure. The concentrations and intrinsic activity of the metal and acid sites, and in particular, their localization are of utmost importance for the catalyst activity, selectivity and stability [20-26]. The reaction selectivity is often affected by the so called ñsite intimacyò [21]. Moreover, for many reactions, the presence of metal nanoparticles on the zeolite external surface can be undesirable and even detrimental for the catalytic performance.

Conventional synthesis methods of metal zeolite catalysts involve impregnation with metal salts and mechanical mixing. Mechanical mixing of a zeolite with a metal catalyst leads to the preferential localization of the metal component outside the zeolite crystallites. During impregnation, the distribution of cations inside the zeolite depends on their diffusivity [27]. Because of a larger solvating shell, diffusion of multi-charged ions inside the micropores can be rather slow. In all catalysts prepared by impregnation, a considerable amount of metal ions can be still found on the zeolite external surface.

Several methods have been proposed to synthetize metal-zeolite composite catalysts with metal nanoparticles encapsulated in the zeolite crystals and located next to the acid sites. Tsubaki and co-workers [28] designed a coreï shell catalyst with a cobalt catalyst in the core and an acidic zeolite membrane on the surface as the shell. The thin zeolite layer on the surface of metallic catalyst does not however, provide the intimacy required for conducting efficient acid-catalysed reactions and may lead to significant diffusion limitations. A rather sophisticated synthetic approach has been recently developed based on the zeolite recrystallization [29, 30]. A complex procedure making use of tetraethylammonium halide salts and halogens has been developed for extraction of Pt nanoparticles from the external surface of zeolites [31]. For specifically synthetized single crystal zeolite ñnanoboxesò a research group in Lyon has developed an extraction method using citric acid [32]. The apparent isolation of metal nanoparticles and acid sites could limit the application of ñnanoboxesò in bifunctional catalysis, where the intimacy between the metal and acid sites is usually required. Therefore, the methods for the design of metal zeolite composite catalysts with metal nanoparticles localized inside zeolite pores in close proximity to the acid sites are still highly desirable. Our group has recently proposed a method [26] for the extraction of cobalt ions from the cobalt zeolite Fischer-Tropsch catalysts using larger

Keggin-type tungstophosphoric acid. Utilizing heteropolyacids for such extraction may represent, however, some risk due to possible catalyst contamination by insoluble oxides, which can be generated during anion hydrolysis.

This paper presents a new approach to the synthesis of nickel-zeolite composite catalysts selectively containing metal nanoparticles in the zeolite micropores using extraction with an organic acid, poly-4-styrenesulfonic acid (PSSA, M_w=70,000-80,000).

The controlled localization of metal nanoparticles either exclusively in the zeolite micropores or also on the zeolite external surface produces strong steric effects on the catalytic performance in the hydrogenation of 1,3,5-tri-isopropyl benzene (TIPB) and toluene over these catalysts.

Materials and methods

Material preparation

The ZSM-5 and BEA commercial zeolites with Si/Al ratios of 11.5 and 12.5 (CBV2314 and CP814E), respectively, were provided by Zeolyst. The Ni-containing zeolites were prepared by incipient wetness impregnation of the ZSM-5 and BEA zeolites with $Ni(NO_3)_2 \cdot 6H_2O$. The Ni content was 16 wt. %. The prepared catalysts were dried in an oven and calcined in air at 450°C.

Poly-4-styrenesulfonic acid (PSSA, M_w=70,000-80,000) with strong acidity and high stability was used for the extraction of nickel and other atoms from the external surface of zeolites. This acid has relatively large anions. For nickel extraction, 0.5 g of the selected catalyst was treated in 13 g (18% wt.% solution in water) of PSSA at 100°C under reflux for 6 h. After the extraction, the nickel zeolite catalyst was carefully washed, dried and again calcined in air at 550°C.

Characterization

The sample chemical composition was determined by X-ray fluorescence (XRF) using a M4 TORNADO (Bruker) spectrometer. The instrument was equipped with 2 anodes, a rhodium X-ray tube (50 kV/600 mA, 30 W) and a tungsten X-Ray tube (50 kV/700 mA, 35 W), and a Silicon-Drift-Detector Si(Li) (<145 eV resolution at 100000 cps (Mn KŬ) with a Peltier cooling to 253°C). For sample characterization, the rhodium X-rays with a poly-capillary lens enabling excitation of an area of 200 εm were used. The measurements were conducted under vacuum (20 mbar). Quantitative analysis was performed using fundamental parameter (FP, standardless).

The apparent surface areas of the catalysts should be calculated using the BET model for the P/Po relative nitrogen pressure <0.04. The BET surface area, pore volume, and average pore diameter were determined by low-temperature nitrogen adsorption using a Micromeritics ASAP 2000 automated system. The samples were degassed under vacuum at <10 mmHg at 300°C for 4 h before N_2 physisorption. The total pore volume (TPV) was calculated from the amount of vapor adsorbed at a relative pressure close to unity by assuming that the pores are completely filled with the condensate in the liquid state. The catalyst external surface area and micropore volume were calculated using the deBoer t-plot method.

The samples were characterized by X-ray diffraction (XRD) using a D8 Advance diffractometer equipped with an energy dispersive detector and a monochromatic CuKŬ radiation source. The samples were analyzed using a step of 0.02° with an acquisition time of 0.5 s. The average size of nickel oxide (NiO) crystallites was determined by the Scherrer equation. Previously it was shown however that it is decomposition of metal precursors and catalyst calcination that generate nickel crystallites and dispersion in the reduced catalysts [33]

The XPS spectra were obtained using a Kratos Axis spectrometer, equipped with an aluminium monochromator for a 1486.6 eV source operating at 120 W. All spectra were recorded under a vacuum of 10^{-8} Torr and recalibrated afterwards with the binding energy of the Al 2p at 74.6 eV.

The catalyst reducibility was examined by temperature-programmed reduction (TPR) performed in an AutoChem II 2920 apparatus (Micromeritics). The samples were reduced in a flow of 5 % H_2/Ar flow (60 ml/min) and heated up to 900^{o}C with a ramp rate of 10 C/min.

The TEM images were taken using a Tecnai instrument equipped with a LaB6 crystal operated at 200 kV. Before the analysis, the samples were dispersed by ultrasound in ethanol for 5 min, and a drop of the suspension was deposited onto a carbon membrane supported on a 300 mesh copper grid.

Comparative characterization of the Brønsted and Lewis acid sites in zeolites, was carried out using transmittance FTIR measurements in the 6000-900 cm^{-1} spectral range utilizing pyridine adsorption. FTIR transmittance measurements were performed at ~80°C using catalyst self-supported disks activated inside an in situ IR cell at 450°C for 5 h in vacuum (10^{-5} Torr, the temperature ramp of 1oC/min). FTIR spectra have been collected using a Thermo iS10 spectrometer at a 4 cm^{-1} resolution (0.96 cm^{-1} data spacing). The spectra were analyzed using specialized Thermo software, Omnic. An excess of Py was admitted into the transmittance cell at 150°C, in a stepwise manner until no changes were observed in the spectra. The saturated sample was then evacuated for 20 min at 150°C to remove physically adsorbed Py. To quantify the number of acid sites from the area of the corresponding IR peaks, the following values of the molar absorption coefficients were used: Ů(B, ZSM-5)=1.08 and Ů(B, BEA)=1.16 for Brønsted acid sites (peak at ~1546 cm^{-1}) and Ů(L)=1.71 cm mol^{-1} for Lewis acid sites (peaks at ~1455-1445 cm^{-1}).

147 *Catalytic tests in the toluene and 1,3, 5-tri-isopropylbenzene (TIPB) conversion*

148 All catalytic experiments were conducted in a 20 mL stainless steel batch autoclave. Prior to the
149 catalytic tests, all the samples were activated in a flow of H_2 at atmospheric pressure during 7 h at
150 400 C. Then, the reduced catalysts were cooled down to room temperature and transferred under
151 argon to the autoclave reactors filled with liquid toluene or 1,3,5-tri-isopropylbenzene (TIPB). In
152 a toluene hydrogenation experiment, 0.015 g of the catalyst was added to 0.2 g of toluene. In the
153 TIPB hydrogenation, the catalyst amount was 0.05 g. The reactor was filled with 0.2 g TIPB. After
154 adding the catalyst and relevant substrate, the reactor was purged and then pressurized to 20 bar
155 with hydrogen. The temperature and reaction time were respectively 150° and 1 h for toluene
156 conversion and 180°C and 3 h for the TIPB hydrogenation. The reaction products were analyzed
157 using a gas chromatograph (Bruker GC-450) equipped with a flame ionization detector (FID) using
158 CP-Sil 5 CB column. The identification of the reaction products was further confirmed using GS-
159 MS analysis.

160 **Results and Discussion**

161 *Catalyst characterization*

162 The TEM images of the Ni/ZSM-5 and Ni/BEA catalysts are shown in **Figure 1**. The
163 commercial ZSM-5 and BEA zeolites contain zeolite agglomerates constituted by relatively
164 small nanosized zeolite crystallites. In the Ni/ZSM-5 prepared by impregnation, the zeolite
165 particles are covered by large agglomerates of nickel oxide nanoparticles (100ï 200 nm,
166 **Figure 1a**). A significant enrichment of the ZSM-5 zeolite external surface with nickel is
167 indicative of its preferential localization outside the zeolite crystallites. Indeed, low
168 diffusivity of hydrated bivalent Ni^{2+} cations limits their access to the ZSM-5 zeolite
169 micropores during the conventional impregnation [27].

Interestingly, very few nickel agglomerates or nanoparticles were detected on the outer surface of the same metal zeolite catalysts after treatment with PSSA (**Figure 1b**). This suggests that nickel oxide nanoparticles located on the zeolite external surface were almost completely removed by PSSA. This observation is consistent with the results of the XRF analysis (**Table 1**), which also show a significant decrease in the nickel content in the ZSM-5 zeolites subjected to extraction with PSSA.

In the Ni/BEA zeolite prepared by impregnation, nickel is uniformly distributed between micropores and zeolite outer surface. Indeed, no nickel oxide clusters were detected by TEM on the outer surface of the Ni/BEA sample (**Figure 1c**). Nickel seems be localized inside of the zeolite micropores. Treatment of Ni/BEA zeolite with PSSA does not results in any noticeable modification of nickel distribution (**Figure 1d**).

ZSM-5 contains relatively small micropores (diameter ~0.55 nm) and slow diffusion of nickel cations during the impregnation leads to nickel preferential localisation on the surface of crystallites. Note that almost no decrease in the nickel content was observed for the BEA zeolite. The BEA zeolite has larger micropores (0.76 × 0.64 nm) compared to the ZSM-5 counterpart and a more open structure. This could lead to a higher fraction of nickel ions inside the micropores of BEA zeolite in comparison with ZSM-5. Previously, we found [10, 26] using a combination of characterisation techniques, rather uniform distribution of cobalt between the BEA zeolite micropores and external surface in the catalysts prepared by incipient wetness impregnation.

The treatment of Ni/BEA with PSSA leads to a major decrease in the concentration of aluminium ions in the BEA zeolite, whilst the aluminium content is almost unaffected by the extraction with PSSA in ZSM-5. Because of the structural features of the BEA zeolite (larger pores and open structure), PSSA can enter the zeolite micropores and selectively

194 extract aluminium ions at least in the zeolite pore mouths, whereas the micropores of ZSM-
195 5 zeolites are inaccessible for this bulky acid. Note that extraction of aluminium from the
196 BEA zeolite can be also facilitated by the relatively smaller zeolite crystallite size and
197 presence of structural defects.
198 The N_2 adsorptionï desorption isotherms of the parent zeolites and nickel zeolite catalysts
199 before and after the PSSA extraction are shown in **Figure 2**. The BEA zeolite exhibits a
200 type I isotherm with an H4 hysteresis [34] at higher relative pressure ($P/P_0 > 0.7$). This
201 hysteresis loop is probably due to the filling of inter-crystalline spaces between relatively
202 small BEA crystallites. The ZSM-5 samples display type I isotherms characteristic of
203 microporous materials. Impregnation with Ni results in a decrease in the amount of adsorbed
204 nitrogen for both zeolites. Impregnation of ZSM-5 zeolites also results in a broad hysteresis
205 loop, which could be related to the formation of mesopores. This mesoporosity is probably
206 related to the agglomeration of individual zeolite crystallites during impregnation and
207 extraction, which creates voids between the zeolite crystallites with a broader pore size
208 distribution.
209 Impregnation with Ni leads to a significant decrease in the zeolite surface area and both
210 mesoporous and microporous volumes (**Table 1**). Note that in addition to the NiO
211 nanoparticles on the zeolite external surface, the impregnated samples also contain nickel
212 species inside the zeolite pores. Therefore, the observed decrease in microporous volume
213 can be due to the localization of nickel inside the zeolite. Because of possible pore blocking,
214 the decrease in the microporous volume, however, is not necessarily directly proportional
215 to the amount of nickel ions located inside of the zeolite crystallites. After the impregnation
216 with nickel nitrate, the decrease in microporous volume is more pronounced in BEA (21%)
217 than in ZSM-5 (~12%). Importantly, the subsequent catalyst exposure to PSSA does not

lead to any noticeable recovery of the microporous volume. Indeed, PSSA mostly extracts nickel species from the zeolite external surface without removing nickel ions from the micropores of ZSM-5 zeolites.

The XRD patterns of the studied catalysts are shown in **Figure S1**, **Supplementary Information** (**SI**), the patterns are offset for clarity. The profiles of the ZSM-5 and relevant nickel catalysts present XRD peaks characteristic of the MFI structure. The samples prepared using BEA zeolites display intense XRD patterns of the beta zeolite, corresponding to materials comprising ~50% of polymorph A and 50% of polymorph B [35]. In addition to the zeolites, crystalline cubic nickel oxide was identified in all nickel zeolite catalysts by the reflections at 37.3°, 43.3°, 62.9°, 75.4°, 79.3° 2ɗ (JCPDS card No. 78-0643). The NiO crystallite size calculated by the Scherrer equation (**Table 1**) was between 15 and 22 nm. These NiO crystallite sizes are much larger than the dimeter of the zeolites micropores. This suggests that a part of nickel is present as relatively large oxide crystallites located on the zeolite external surface. The treatment of BEA and ZSM-5 zeolite with PSSA results in modification of XRD patterns. In the case of BEA, only small decreases in the intensity of XRD peaks of NiO and in the Ni contents in the catalysts were observed. In the case of ZSM-5, much more significant decreases in the intensity of NiO XRD peaks and Ni content in the samples was observed. This suggests a clear Ni removal during extraction with PSSA. The results are also consistent with SEM data which showed removal of NiO crystallites from the outré sauce of ZSM-5 zeolite during the extraction (**Figure 1a and b**).

The TPR profiles of the nickel zeolite catalysts (**Figure 3**) exhibit broad hydrogen consumption peaks in the temperature range from 350 to 700°C. Previous reports [36, 37] suggest that pure NiO shows a single TPR peak at about 400°C. Thus, the low temperature peaks located between 400 and 500°C may correspond to the reduction of NiO particles.

242 Note that because of diffusional limitations during the reduction, nickel oxide clusters
243 located in zeolite pores may have slightly higher reduction temperature [38]. In addition to
244 the low temperature peaks observed at 420-450°C, TPR profiles of the nickel catalysts
245 prepared from the ZSM-5 zeolite exhibit low intensity peaks at 520-550°C. There are two
246 possible interpretations of these peaks. First, these peaks can be attributed to the presence
247 of nickel phyllosilicate species, as was suggested previously [37, 39, 40]. Generally, nickel
248 phyllosilicate is not observed by XRD probably due to its very high dispersion. High
249 temperature TPR peaks can be also attributed to the reduction of highly dispersed nickel
250 species [38, 41]. These dispersed nickels species can be either isolated Ni ions in the cationic
251 sites of ZSM-5 and BEA zeolites or extremely small nickel oligomeric species in the zeolite
252 micropores [38]. Interestingly, the variation in the intensity of TPR peaks after Ni extraction
253 correlates with the amount of nickel in the catalysts (**Table 1**). Integration of TPR profiles
254 (**Table 2**) suggests a relatively high extent of nickel reduction in all zeolite catalysts (>80
255 %). Thus, all nickel in the catalysts is reducible at temperatures lower than 600-700°C. This
256 is also indicative of a relatively low concentration of hardy reducible nickel silicate or
257 aluminates. The total intensity of the TPR peaks for Ni/BEA and Ni/BEA AT is only slightly
258 affected by the extraction, but their shape changes dramatically (**Figure 3**). Indeed, nickel
259 in the BEA zeolite is largely located inside the zeolite pores and the total amount of nickel
260 is almost unaffected by this treatment (**Table 1**). At the same time, the intensity of high
261 temperature peaks decreases and those of the low temperature peaks increases, which is
262 indicative of the decrease in the concentration of Ni^{2+} ions in the cationic positions of BEA
263 and formation of larger nickel oxide clusters. This is consistent with the significant decrease
264 in the aluminium content in the BEA zeolite following the acid treatment. Indeed, the
265 Brønsted acid sites in zeolites are associated with the bridging Si-OH-Al groups and the

observed decrease in the aluminium concentration in BEA would coincide with the decrease in the number of cationic sites. This would favour sintering of isolated Ni^{2+} ions or oligomeric nickel species into larger NiO clusters.

Some decrease in the intensity of TPR peaks, which are shifted to lower temperatures after nickel extraction, is observed for Ni/ZSM-5. The lower intensity of TPR peaks in Ni/ZSM-5 AT corresponds to a decrease in the Ni content in the acid-treated samples from 16.7 to 12.8 wt %. The shift of TPR peaks to lower temperature suggests agglomeration of highly dispersed nickel species into larger nickel oxide particles located in the zeolite pores.

The Ni 2p XPS spectra are displayed in **Figure 4**. The nickel XPS spectrum can be divided into two regions by spin-orbit coupling, referred to as $2p_{1/2}$ (å 870ï 885 eV) and $2p_{3/2}$ (å 845ï 865 eV) edges [42-44]. These are accompanied by ñshakeupò satellite bands ~1.5 eV and ~7 eV higher in binding energy relative to the main lines. The amplitude and exact location of satellite and principal peaks depend on the nickel oxidation state and coordination [45]. The XPS spectra confirm that nickel is present in its divalent form [46]. The shoulder close to the main line suggests that in ZSM-5 nickel is mostly in octahedral coordination, similar to that in NiO. In the BEA zeolite, nickel coordination could be more distorted [45, 46].

The atomic concentration ratios for Ni, Si and Al measured by XPS are given in **Table 2**. Extraction using PSSA results in a significant decrease in the concentration of aluminium in BEA zeolite. The Si/Al and Ni/Si ratios for this zeolite calculated from the XPS data are consistent with XRF. Note that the amount of nickel only slightly decreases in BEA after extraction. The Si/Al ratios in Ni/BEA and Ni/ZSM-5 zeolites are also rather close to the bulk values measured by XRF. Ni/ZSM-5 catalysts show a significant surface dealumination, whereas the $(Si/Al)_{XRF}$ bulk ratio remains almost unchanged. Nickel oxide

crystallites were detected by TEM on the outer surface of Ni/ZSM-5 sample (**Figure 1a**). These crystallites are removed after extraction with PSSA (**Figure 1b**). The microscopy results are also consistent with XPS, which indicated an increase in nickel concentration of the outer surface of ZSM-5 zeolite. The phenomena are much complex with BEA zeolite. In this zeolite, extraction with PSSA results in partial dealumination.

The acidity of nickel zeolite catalysts was evaluated using pyridine (Py) adsorption monitored by FTIR spectroscopy. The relevant FTIR spectra are shown in **Figure 5** (the spectra are offset for clarity). After Py adsorption, BEA and ZSM-5 zeolites exhibit characteristic bands at ~1545 and 1456 cm^{-1} attributed respectively to the pyridinium ion (PyH^+) adsorbed on Brønsted acid sites (BAS) and to the Py molecules coordinated to Lewis acid sites (LAS). Py adsorbed on both LAS and BAS also displays a band at ~1490 cm^{-1}. **Table 2** shows the concentration of BAS and LAS calculated from the intensity of the FTIR bands at ~1545 and 1456 cm^{-1}. The amount of BAS (Py-BAS complexes) significantly decreases in all zeolites after impregnation with the Ni^{2+} ions owing to nickel ion exchange with the protons of the bridged hydroxyl groups. At the same time, the concentration of LAS (Py-LAS complexes) increases. In addition, the Py-LAS peak shifts from 1456 to 1450 cm^{-1}. This can be explained by Py adsorption on LAS of the zeolites, associated with extraframework aluminium, $(Al)_{ex}$ and LAS associated with the introduced Ni^{2+} ions. The fractions of Py adsorbed on different types of LAS can be calculated using spectral deconvolution (Table 2). Examples of the deconvolution are given in **Figure S2, SI**. The concentration of Py adsorbed on Ni^{2+} ions also provides information about the relative fraction of Ni^{2+} in the zeolite cationic positions (**Table 2**). The extraction with PSSA leads on the one hand to decrease in the concentration of Ni^{2+} ions in BEA zeolite. The treatment of BEA zeolite with PSSA leads also to partial dealumination and an increase in the Si/Al

ratio. Consequently, the concentrations of BAS and LAS significantly decrease (**Table 2).** This is probably due to the drop in the concentration of the aluminium and agglomeration of Ni^{2+} into larger NiO particles. On the other hand, the fraction of the Ni^{2+} ions increases in the ZSM-5 after extraction. Indeed, mostly nickel oxide particles from the ZSM-5 zeolite outer surface are removed by extraction, whereas the isolated Ni^{2+} ions inside the zeolite micropores are not affected by this treatment.

In BEA, the BAS concentration drops significantly after the extraction. These results are in good agreement with elemental analysis, which demonstrates that ~80% of Al is removed in the PSSA treated Ni/BEA (**Table 1**). In both the ZSM-5 samples, the extraction leads to the removal of nickel from the zeolite, whilst FTIR indicates only a slight increase in the concentration of BAS and LAS in the extracted catalysts, which can be attributed to the loss of mostly NiO species and Ni^{2+} ions from the zeolite outer surface. A major decrease in the concentration of both BAS and LAS is observed in the BEA zeolite after the PSSA extraction. Because of the larger pores and a greater number of defect sites in the BEA structure, PSSA can extract aluminium ions from the zeolite framework. At the same time, Ni species in the pores of the BEA zeolites coalesce into relatively larger NiO clusters leading to much smaller fraction of Ni^{2+} ions interacting with Py. The amount of Py adsorbed over isolated nickel ions drops significantly in the Ni/BEA zeolite (**Table 2**). This seems to be due to the extraction of aluminium from the zeolite, which results in the decrease in the concertation of the bridging hydroxyl groups and consequent agglomeration of NiO species. Interestingly, a very slight effect of the extraction was observed on the amount of isolated Ni^{2+} species in the ZSM-5 zeolites. Indeed, isolated Ni^{2+} located in the small ZSM-5 micropores cannot be extracted with the bulky PSSA molecules.

Thus, the characterization suggests a strong influence of the impregnation with nickel and extraction with PSSA on the structure of nickel containing zeolite catalysts. XRD analysis indicates that the zeolite crystalline structure is not altered to any noticeable extent by the impregnation and extraction. Larger pores of the BEA zeolite facilitate nickel migration inside the zeolite micropores and ion exchange. Consequently, the impregnated BEA zeolite contains a higher fraction of nickel ions in the zeolite micropores compared to the ZSM-5 counterpart. The acid treatment of the BEA zeolite leads to selective extraction of aluminium ions from the zeolite crystallites. As a result, the Si/Al ratio in BEA increases very significantly after the extraction (from 11.2 to 44, **Table 2**). Hence, the concentrations of BAS and LAS significantly decrease in Ni/BEA AT. Isolated Ni^{2+} ions and very small oligomeric species present in Ni/BEA agglomerate after extraction into larger NiO clusters. The situation is very different for the ZSM-5 zeolites, which have micropores smaller than those in BEA. Smaller micropores make it difficult for nickel ions to migrate into the zeolite and to undergo ion exchange with the zeolite hydroxyl groups. Hence, ZSM-5 zeolites after impregnation with nickel nitrate contain a higher fraction of nickel on the zeolite external surface, which is mostly present as NiO according to XPS and XRD. A higher fraction of nickel on the zeolite external surface was detected by TEM and XPS (**Table 2**) in the ZSM-5 samples. Impregnation with nickel also results in a decrease in the number of BAS because of the partial ion exchange with Ni^{2+}, although it is much smaller than that for BEA zeolite. Extraction with PSSA strongly reduces the amount of nickel on the external surface of the ZSM-5 zeolites. The PSSA molecules do not enter the micropores of ZSM-5 zeolite, which are smaller than the pores in BEA, and almost do not extract aluminium ions. The slight increase in the concentration of BAS observed after the extraction can be attributed to the removal of Ni^{2+} species from the zeolite cationic sites located mostly on the external surface.

To summarize, the impregnated Ni/BEA zeolite contains Ni^{2+} ions both on the external surface and in the zeolite micropores, while a higher fraction of nickel is localized on the external surface of the Ni/ZSM-5 zeolite. The nickel on the zeolite external surface of ZSM-5 zeolites is mostly present in the form of NiO clusters. The PSSA treatment performed with Ni/BEA zeolite leads to the extraction of aluminum ions from the zeolite crystallites and a significant increase in the Si/Al ratio. Because of the insufficient number of BAS, Ni species in the BEA zeolite during the extraction agglomerate into larger NiO clusters. The impregnated ZSM-5 zeolites contain larger NiO particles on the external surface and a small amount of nickel in micropores. The extraction results in the removal of nickel from the zeolite external surface and some agglomeration of Ni species inside the zeolite micropores may also occur.

Catalytic tests in toluene and 1,3,5 tri-isopropyl benzene (TIPB) conversion

Hydrogenation of TIPB was used as a model reaction for the nickel active sites on the zeolite external surface. The size of this molecule is greater than the pore sizes of ZSM-5 and even BEA zeolites. Thus, TIPB cannot react on the active sites inside the crystallites of these two zeolites.

Previously, TIPB cracking was used to evaluate the reactivity of the Brønsted acid sites on the external surface of Y and ZSM-5 zeolites. This reaction is particularly sensitive to the accessibility of Brønsted acid sites in the mesopores or on the external surface of zeolites. Note that TIPB cracking requires relatively high temperature (about 300°C). Reducing the crystal size of the HY and H-ZSM-5 zeolites [47], using mesoporous hierarchical zeolites [48, 49] or composites [50, 51] leads to a significant increase in the rate of TIPB cracking. In the present work, we used TIPB hydrogenation conducted at 180°C in order to evaluate

385 the localization of nickel metal sites in the BEA and ZSM-5 zeolites. The catalytic data are
386 presented in **Tables 3 and 4**. Under the reaction conditions, the only product of TIPB
387 hydrogenation was the corresponding tri-isopropyl cyclohexane. In the catalysts prepared
388 by impregnation, the highest conversion was observed over the Ni/BEA zeolites (**Table 3**).
389 The concentration of nickel sites on the zeolite external surface depends on zeolite
390 crystallite size, nickel dispersion, reducibility and its distribution between the external
391 surface and micropores. In the impregnated catalysts, the hydrogenation rate seems to
392 depend on the size of zeolite crystallite. After the PSSA treatment, the hydrogenation rate
393 drops much more significantly in Ni/ZSM-5, while in Ni/BEA the reaction rate decreases
394 to a lesser extent and it still remains the most active catalyst. NTY is defined as
395 hydrogenation rate normalized by the nickel content in the catalysts. Note that a significant
396 decrease in the TIPB nickel time yield (NTY) after extraction occurred over ZSM-5 zeolite
397 from 327 to 108×10^{-6} s^{-1} (**Table 3**). Indeed the reaction occurs on the outer surface of the
398 zeolite. PSSA extraction reduces the concentration of the nickel sites on the outer surface
399 and thus the rate of hydrogenation of TIPB, which is a large molecule. The decrease in NTY
400 is less significant over BEA because of more open zeolite structure, larger pore diameter
401 and significant mesoporous volume (**Tables 1 and 3**).
402 The catalytic performance of the prepared materials was also evaluated in toluene
403 conversion (**Table 4**). Toluene is a much smaller molecule than TIPB and should access
404 active sites located on the outer surface and inside the pores of the BEA and ZSM-5 zeolites.
405 The removal of nickel from the zeolite external surface via extraction with PSSA leads to a
406 decrease in the number of metal sites. The remaining metal hydrogenation sites are then
407 located mostly inside the zeolite pores. Interestingly, different to the hydrogenation of
408 TIPB, the toluene hydrogenation rate remains mostly proportional to the overall nickel

content and toluene NTY is not much affected by PSSA extraction and remains about ~5 $x10^{-3}$ s^{-1} (**Table 4**). This suggests that nickel active sites located on the zeolite outer surface and in the zeolite micropores have almost the same intrinsic activity in toluene hydrogenation. **Figure 6** shows the ratio of NTY for TIPB and toluene for the nickel zeolite catalysts. This ratio drops drastically after extraction. This is indicative of much more significant decrease in the rate of TIPB hydrogenation compared to toluene, which is likely to be due a much greater drop in the concentration of the nickel on the zeolite outer surface compared to the zeolite micropores. The catalytic data are therefore consistent with the characterization results, which suggest selective removal of nickel ions after the catalyst treatment with PSSA. The proposed strategy for the synthesis of the composites containing metal exclusively in the zeolite micropores can be extended for the design of numerous metal zeolite composite catalysts.

Conclusions

Extraction of nickel ions from the zeolite external surface using PSSA is highly efficient for the synthesis of metal-zeolite composite catalysts selectively containing metal species inside the zeolite micropores. The method is particularly suitable for the ZSM-5 zeolites, whereas for the BEA based catalysts. Unexpectedly, thermal treatment of zeolite materials with PSSA may lead to more complex phenomena than simple selective removal of part of NiO particles, including partial dealumination, which may decrease sintering resistance, and influence catalytic acid-base properties. Such effect can be related to the porous nature of zeolites.

Nickel extraction from the zeolite external surface results in a major decrease in the hydrogenation rate and nickel time yield for bulky TIPB, while the toluene hydrogenation

rate remains largely proportional to the nickel content in the zeolites containing nickel on the zeolite outer surface and in the micropores. The described approach can be extended to a wide range of microporous materials and can be used to enhance numerous catalytic reactions, which occur on metal nanoparticles in the zeolite micropores.

Acknowledgements

The authors are grateful to Olivier Gardoll, Laurence Burylo, Pardis Simon, Martine Frère and Debora Strossi for help with TPR, XRD, XPS and TEM measurements. The authors thank International Cooperation Program CAPES/COFECUB Foundation funded by CAPES ï Brazilian Federal Agency for Support and Evaluation of Graduate Education within the Ministry of Education of Brazil for providing PhD stipends and financial support for this work. The authors acknowledge financial support of the French National Research Agency (DirectSynBioFuel project, Ref. ANR-15-CE06-0004 and NANO4-FUT, Ref. ANR-16-CE06-0013). The authors acknowledge financial support from the European Union (Interreg V project PSYCHE).

Conflicts of interest

No conflicts of interest to declare.

References

1 Guisnet M, Gilson, J-P (2005) Zeolites for cleaner technologies. Catalytic science series - vol. 3 (Series Editor: G. J. Hutchings), Imperial College Press, London, p.390.

2 Marcilly, C. (2001) Evolution of refining and petrochemicals. What is the place of zeolites? Stud. Surf. Sci. Catal 135:37-60.

3 Corma A, Martinez A (2005) Zeolites in refining and petrochemistry. Stud. Surf. Sci Catal 157: 337-366. .

4 Marcilly, C (2005). Acido-basic catalysis-application to refining and petrochemistry. Technip, Paris.

5 Vermeiren W, Gilson J-P (2009) Impact of Zeolites on the Petroleum and Petrochemical IndustryTop. Catal. 52: 1131-1161

6 Huber GW, Cortright RD, Dumesic J.A (2004) Renewable alkanes by aqueous-phase reforming of biomass-derived oxygenates, Angew. Chem. 43: 1549-1551.

7 Guan G., Kaewpanha M, Hao X., Abudula A. (2016) Catalytic steam reforming of biomass tar: Prospects and challenges. Renew. Sust. Energ. Rev. 58: 450-461.

8 Héroguel F., Rozmysłowicz B., Luterbacher J.S. (2015) Improving Heterogeneous Catalyst Stability for Liquid-phase Biomass Conversion and Reforming. Chimia 69: 582-591.

9 Zhang Q, Cheng K, Kang J, Deng W and Wang Y (2014) Fischerï Tropsch Catalysts for the Production of Hydrocarbon Fuels with High Selectivity. ChemSusChem 7:1251-1264.

10 Subramanian V, Zholobenko VL, Cheng K, Lancelot C, Heyte S, Thuriot J, Paul S, Ordomsky VV, Khodakov AY (2016) The Role of Steric Effects and Acidity in the Direct Synthesis of iso Paraffins from Syngas on Cobalt Zeolite Catalysts. ChemCatChem 8: 380-389.

11 Yang G, Tsubaki N, Shamoto J, Yoneyama Y and Zhang Y (2010) Confinement Effect and Synergistic Function of H-ZSM-5/Cu-ZnO-Al_2O_3 Capsule Catalyst for One-Step Controlled SynthesisJ. Am. Chem. Soc. 132: 8129-8136.

12 Masalska A (2005) Ni-loaded catalyst containing ZSM-5 zeolite for toluene hydrogenation. Appl. Catal. A 294: 260-272.

13 Lee D, Cho S, Kim G-J, Kim H, Lee I-K (2007) Efficient and Selective Hydrogenation of Carboxylic Acid Catalyzed by Ni or Pd on ZSM-5. J. Ind. Eng. Chem. 13:1067.

14 Mihaylov M, Hadjiivanov K. (2004) Redox couples in the selective catalytic reduction of NOx with hydrocarbons over Coï ZSM-5 and Niï ZSM-5 catalysts: an FT-IR study. Chem. Commun. 2200-2201.

15 Badrinarayanan S, Hegde R.I, Balakrishnan I, Kulkarni S.B, Ratnasamy P (1981) XPS study of nickel in NiHZSM5 catalysts. J. Catal. 71: 439-442.

16 Ziebro J, Ğukasiewicz I, Borowiak-Palen E, Michalkiewicz B (2010) Low temperature growth of carbon nanotubes from methane catalytic decomposition over nickel supported on a zeolite. Nanotechnology 21: 145308, 6pp.

17 Finiels A, Fajula F and Hulea V (2014) Nickel-based solid catalysts for ethylene oligomerization ï a review. Catal. Sci. Technol. 4: 2412-2426.

18 Yuan H-X, Xia Q-H, Zhan H-J, Lu X-H, Su K-X (2006) Catalytic oxidation of cyclohexane to cyclohexanone and cyclohexanol by oxygen in a solvent-free system over metal-containing ZSM-5 catalysts. Appl. Catal. A 304:178-184.

19 Vitale G, Molero H, Hernandez E, Aquino S, Birss V, Pereira-Almao P (2013) One-pot preparation and characterization of bifunctional Ni-containing ZSM-5 catalysts. Appl. Catal. A 452: 75-87.

20 Ertl G, Knözinger H, Weitkamp J (1999) in Preparation of solid acids, Wiley-VCH, Germany.

21 .Weisz, PB (1962) Polyfunctional Heterogeneous Catalysis. Adv. Catal. 13: 137-190.

22 Zeļevińć J, Vanbutsele G, de Jong KP, Martens JA (2015) Nanoscale intimacy in bifunctional catalysts for selective conversion of hydrocarbons. Nature 528: 245-248.

23 Samad JE, Blanchard J, Sayag C, Louis C, Regalbuto JR (2016) The controlled synthesis of metal-acid bifunctional catalysts: The effect of metal:acid ratio and metal-acid proximity in Pt silica-alumina catalysts for n-heptane isomerization. J.Catal. 342: 203-212.

24 Prins, R (2012) Hydrogen Spillover. Facts and Fiction. Chem. Rev.112: 2714-2738.

25 Im J, Shin H, Jang H, Kim H, Choi M (2014) Maximizing the catalytic function of hydrogen spillover in platinum-encapsulated aluminosilicates with controlled nanostructures. Nat. Commun 5: Article number: 3370.

26 Carvalho A, Marinova M., Batalha N, Marcilio NR, Khodakov AY and Ordomsky VV (2017) Design of nanocomposites with cobalt encapsulated in the zeolite micropores for selective synthesis of isoparaffins in Fischerï Tropsch reaction. Catal. Sci. Technol. 7: 5019-5027.

27 Stakheev AY, Khodakov AY, Kustov LM, Kazansky VB, Minachev KM (1992) Localization of polyvalent cations in pentasil catalysts modified by metal oxides. Zeolites 12: 866-869.

28 He J, Liu Z, Yoneyama Y, Nishiyama N, Tsubaki N (2006) Multiple Functional Capsule Catalysts: A Tailor Made Confined Reaction Environment for the Direct Synthesis of Middle Isoparaffins from Syngas. Chem. Eur. J. 12: 8296-8304.

29 Li S, Tuel A, Laprune D, Meunier F and Farrusseng D (2015) Transition-Metal Nanoparticles in Hollow Zeolite Single Crystals as Bifunctional and Size-Selective Hydrogenation Catalysts. Chem. Mater 27: 276-282.

30 Goel S, Zones SI, Iglesia E (2014) Encapsulation of Metal Clusters within MFI via Interzeolite Transformations and Direct Hydrothermal Syntheses and Catalytic Consequences of Their Confinement. J. Am. Chem. Soc. 136: 15280-15290.

31 Knapp C, Obuchi A, Uchisawa. JO, Kushiyama S, Avila P (1999) Method for selective removal of supported platinum particles from external zeolite surfaces: characterisation of and application to a catalyst for the selective reduction of nitrogen oxide by hydrocarbons. Microporous & Mesoporous Mater. 31: 23-31.

32 Laprune D, Tuel A, Farrusseng D, Meunier F.C (2017) Selective removal of external Ni nanoparticles on Ni@silicalite-1 single crystal nanoboxes: Application to size-selective arene hydrogenation. Appl. Catal. A 535: 69-76.

33 Munnik, P., De Jongh, P.E., De Jong, K.P. (2015) Recent Developments in the Synthesis of Supported Catalysts. Chemical Reviews 115: 6687-6718.

34 Thommes M, Kaneko K, Neimark AV, Olivier JP, Rodriguez-Reinoso F, Rouquerol J and Sing KSW (2015) Physisorption of gases, with special reference to the evaluation of surface area and pore size distribution (IUPAC Technical Report). Pure Appl. Chem. 87: 1051-.1069.

35 Treacy M.M. Higgins JB (2007) Collection of simulated XRD powder patterns for zeolites. 5th revised edition. Elsevier.

36 Tomiyama S, Takahashi R, Sato S, Sodesawa T, Yoshida S. (2003) Preparation of Ni/SiO_2 catalyst with high thermal stability for CO_2-reforming of CH_4. Appl. Catal. A 241: 349-361.

541 37 Soghrati E, Kay T, Ong C, Poh CK, Kawi S, Borgna A (2018) Zeoliteï supported nickel
542 phyllosilicate catalyst for CO hydrogenolysis of cyclic ethers and polyols. Appl. Catal. B
543 235: 130-142.
544 38 Maia AJ, Louis B, Lam YL, Pereira MM (2010) Ni-ZSM-5 catalysts: Detailed
545 characterization of metal sites for proper catalyst design. J. Catal. 269: 103-109.
546 39 Chen B-H, Chao Z-S, He H, Huang C, Liu Y-J, Yi W-J, Wei X-L, An J-F (2016) Towards
547 a full understanding of the nature of Ni(II) species and hydroxyl groups over highly
548 siliceous HZSM-5 zeolite supported nickel catalysts prepared by a deposition-precipitation
549 method. Dalton Trans. 45: 2720-2739.
550 40 Chen B-H, Liu W, Li A, Liu Y-J, Chao Z-S (2015) A simple and convenient approach for
551 preparing coreï shell-like silica@nickel species nanoparticles: highly efficient and stable
552 catalyst for the dehydrogenation of 1,2-cyclohexanediol to catechol. Dalton Trans 44:
553 1023-1038.
554 41 Romero M.D, de Lucas A, Calles JA, Rodriguez A (1996) Bifunctional catalyst NiHZSM-
555 5: effects of the nickel incorporation method. Appl. Catal. A 146, 425-441.
556 42 Biju V and Abdul Khadar M (2002). Electronic Structure of Nanostructured Nickel Oxide
557 Using Ni 2p XPS Analysis. Journal of Nanoparticle Research 4: 247-253.
558 43 Uhlenbrock S, Scharfschwerdt C, Neumann M, Illing G and Freund H ï J (1992) The
559 influence of defects on the Ni 2p and O 1s XPS of NiO. J. Phys. Condens. Matter 4: 7973-
560 7978.
561 44 Alders D, Voogt FC, Hibma T and Sawatzky GA (1996) Nonlocal screening effects in 2p
562 x-ray photoemission spectroscopy of NiO (100). Phys. Rev. B 54: 7716.

563 45 Lenglet M, DõHuysser A and Jorgensen CK (1987) Optical spectra, x-ray photoelectron
564 spectra and XANES of divalent nickel in mixed spinels $NiFe_{2-x}Cr_xO_4$. Inorganica Chimica
565 Acta 133: 61-65.
566 46 Wrobel G, Sohier MP, DõHuysser A and Bonnelle JP (1993) Hydrogenation catalysts based
567 on nickel and rare earth oxides: Part II: XRD, electron microscopy and XPS studies of the
568 cerium-nickel-oxygen-hydrogen system. Appl. Catal. A 101: 73-93.
569 47 Morales-Pacheco P, Domínguez JM, Bucio L, Alvarez F, Sedran U, Falco M (2011)
570 Synthesis of FAU(Y)- and MFI(ZSM5)-nanosized crystallites for catalytic cracking of
571 1,3,5-triisopropylbenzene. Catal. Today166: 25-38.
572 48 Tarach KA, Góra-Marek K, Martinez-Triguero J, Melián-Cabrera I (2017) Acidity and
573 accessibility studies of desilicated ZSM-5 zeolites in terms of their effectiveness as catalysts
574 in acid-catalyzed cracking processes. Catal. Sci. Technol.7: 858-873.
575 49 Hoan Vu X, Tam Truong T, Armbruster U (2018) Enhanced cracking of bulky
576 hydrocarbons over hierarchical ZSM-5 materials: a comparative study. J. Porous Mater.
577 DOI: 10.1007/s10934-018-0633-0.
578 50 Aghakhani MS, Khodadadi AA, Najafi Sh, Mortazavi Y (2014) Enhanced
579 triisopropylbenzene cracking and suppressed coking on tailored composite of Y-
580 zeolite/amorphous silicaï alumina catalyst. J. Ind. Eng. Chem. 20: 3037-3045.
581 51 Vu XH, Bentrup U, Hunger M, Kraehnert R, Armbruster U, Martin A (2014) Direct
582 synthesis of nanosized-ZSM-5/SBA-15 analog composites from preformed ZSM-5
583 precursors for improved catalytic performance as cracking catalyst. J. Mater. Sci. 49: 5676-
584 5689.
585

586

587

588

589 **Table 1** - Catalyst characterization

	S_{BET}[a] ($m^2.g^{-1}$)	V_{meso}[a] ($cm^3.g^{-1}$)	V_{micro}[a] ($cm^3.g^{-1}$)	V_{micro} decrease %	NiO cryst. size XRD (nm)	XRF Ni (wt.%)
HBEA	710	0.45	0.19		-	-
Ni/BEA	560	0.37	0.15	21	19	17.5
Ni/BEA AT	550	0.41	0.15	24	20	16.3
S-ZSM5	450	0.06	0.13		-	-
Ni/ZSM5	350	0.06	0.12	12	23	16.7
Ni/ZSM5 AT	250	0.05	0.08	37	18	12.8

590 [a] values normalized per gram of activated zeol*i*te

591

592

593 **Table 2 -** Catalyst acidity measured by Py adsorption, Ni/Si and Si/Al ratios measured by XRF and

594 XPS

	Number of acid sites, ε mol.g^{-1}				Ni^{2+}/ Ni_{tot}	XRF		XPS (atomic ratio)		Reducible nickel from TPR[b], %
	BAS[a]	LAS[a]	LAS (Al)ex	LAS Ni^{+2}		Ni/Si	Si/Al	Ni/Si	Si/Al	
HBEA	302	295	295	-	-	-		-	-	-
Ni/BEA	83	372	68	304	10.2	0.54	11.2	0.07	11.7	82
Ni/BEA AT	48	30	1	28	1.0	0.46	44.0	0.05	51.0	95
HZSM-5	720	93	93	-		-	9.3	-	-	-
Ni/ZSM-5	161	347	82	265	9.3	0.51	10,6	0.43	10.3	84
Ni/ZSM-5 AT	205	332	82	250	11.4	0.36	11.4	0.40	16.4	80

595 [a] obtained by IR spectroscopy with pyridine adsorption at 150°C

596 [b] calculated from TPR profiles

597

Table 3 -Catalytic performance in conversion of TIPB (T = 180 °C, P = 20 bar, t = 3 h).

Catalyst	Rate, ε mol/g_{cat}/s	NTY, 10^{-6} s^{-1}	X, %
Ni/BEA	1.5	501	82
Ni/BEA AT	0.8	296	45
NI/ZSM-5	0.9	327	51
Ni/ZSM-5 AT	0.2	108	13

Table 4 - Catalytic performance in conversion of toluene (T = 150 °C, P = 20 bar).

	Rate, ε mol/g_{cat}/s	NTY*, 10^{-3} s^{-1}	Reaction time, h	X,%
Ni/BEA	11.7	3.94	1	29
Ni/BEA AT	17.3	6.27	1	43
Ni/ZSM-5	14.1	4.98	1	35
			2	60
			2.5	77
Ni/ZSM-5 AT	11.7	5.38	1	29
			1.5	40

*NTY was calculated from catalytic data aftre1 h of reaction

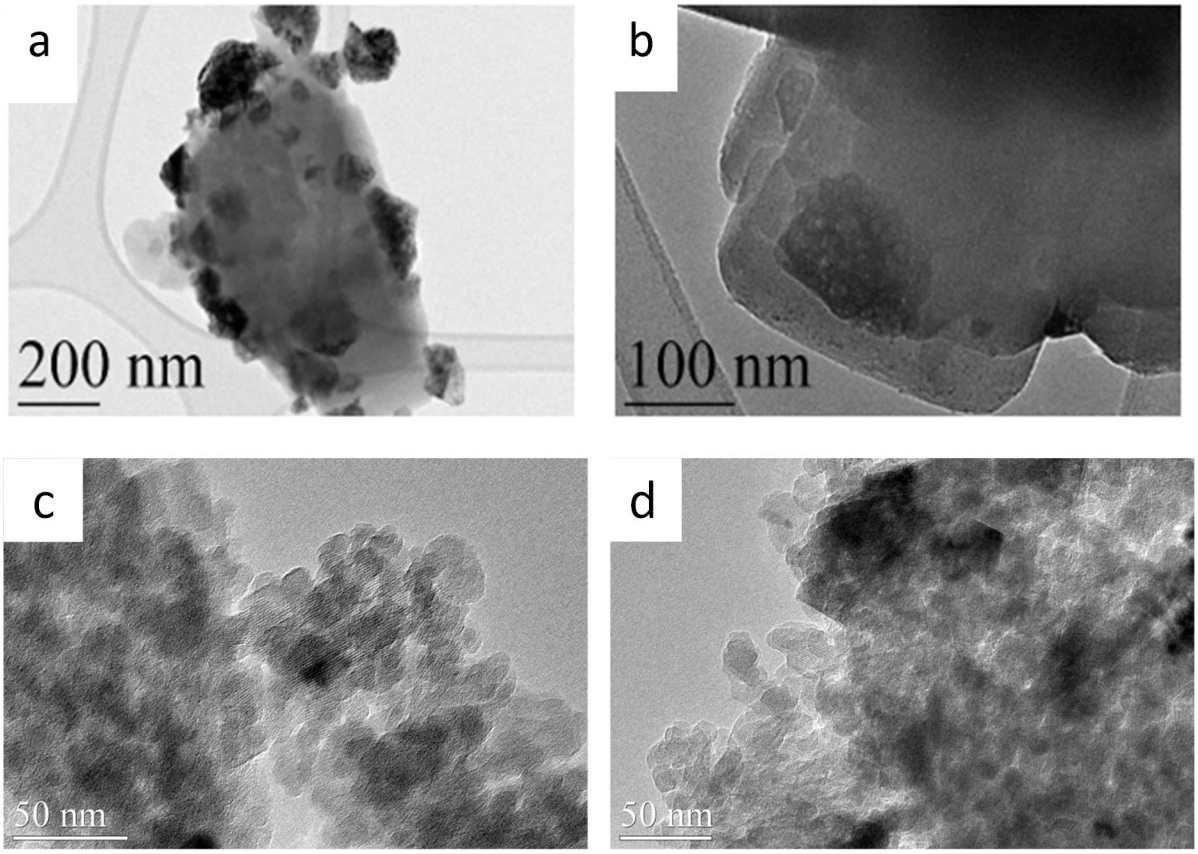

Figure 1. TEM images of the Ni/ZSM-5 (a), Ni/ZSM5 AT (b), Ni/BEA (c) and Ni/BEA AT (d) catalysts before and after nickel extraction with PSSA.

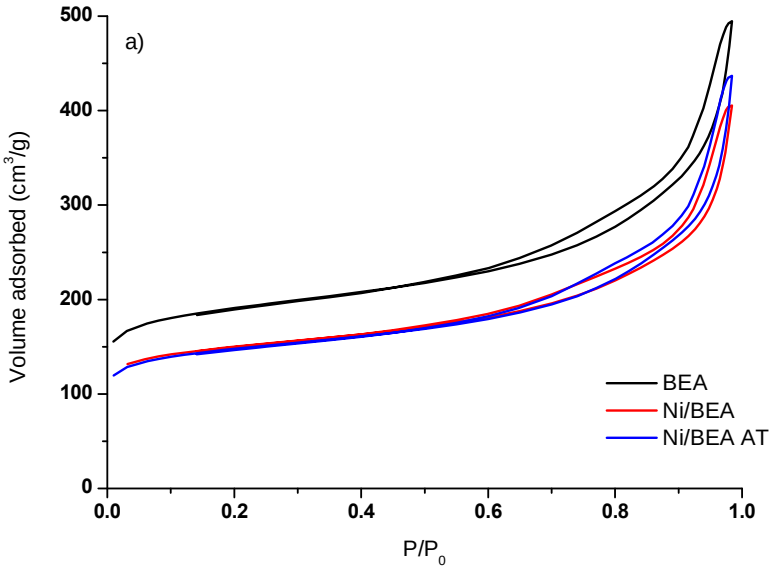

624

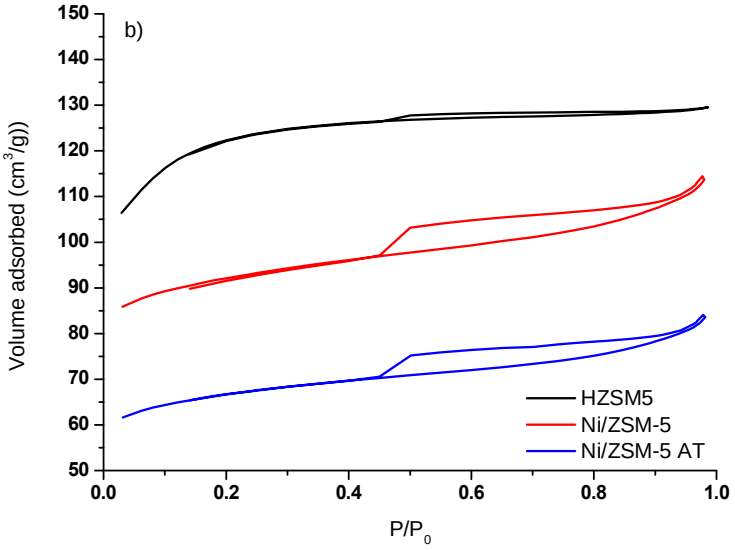

625

626

627 **Figure 2** ï Nitrogen adsorption-desorption isotherms of the zeolite and nickel zeolite catalysts
628 before and after treatment with PSSA: a BEA; b ZSM-5.

629

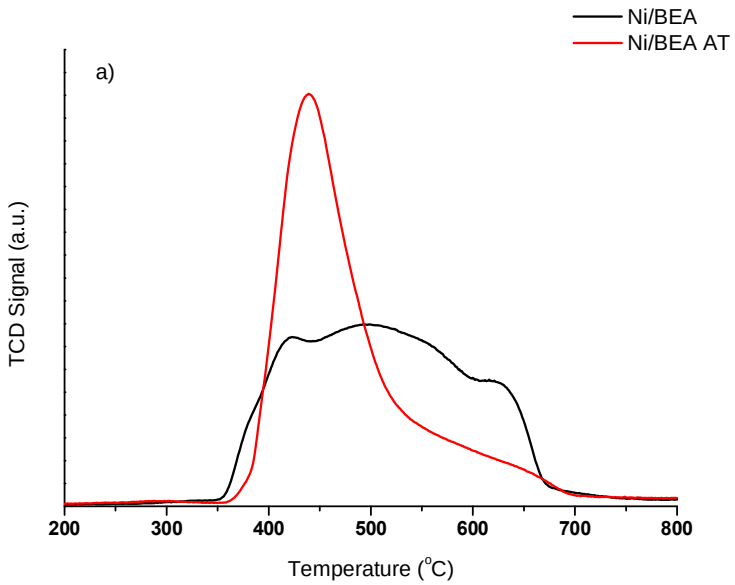

630

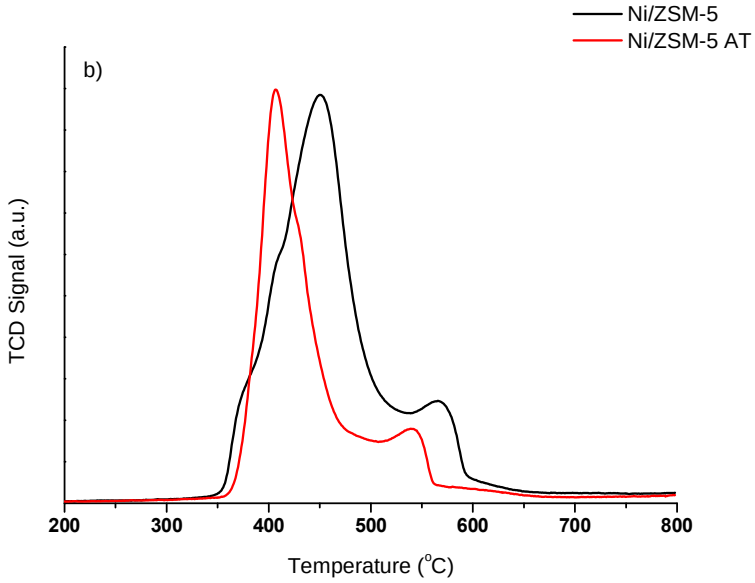

631

632 **Figure 3** ï TPR profiles of Ni/zeolite catalysts before and after treatment with PSSA: a BEA; b
633 ZSM-5.

634

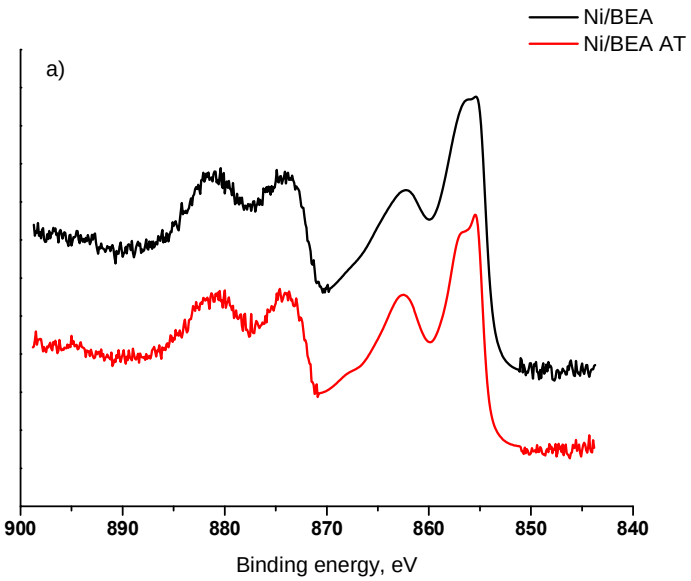

635

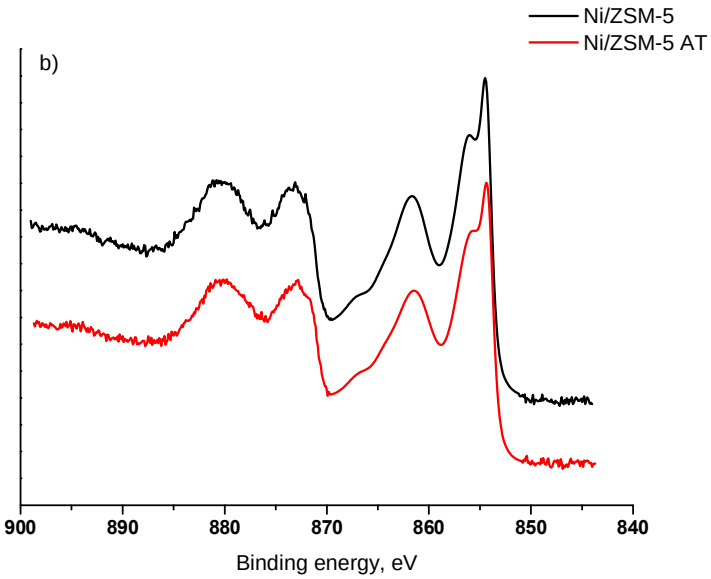

636

637 **Figure 4** ï Ni 2p XPS spectra of the Ni/zeolites before and after treatment with PSS: a BEA; b
638 ZSM-5.

639

640

641

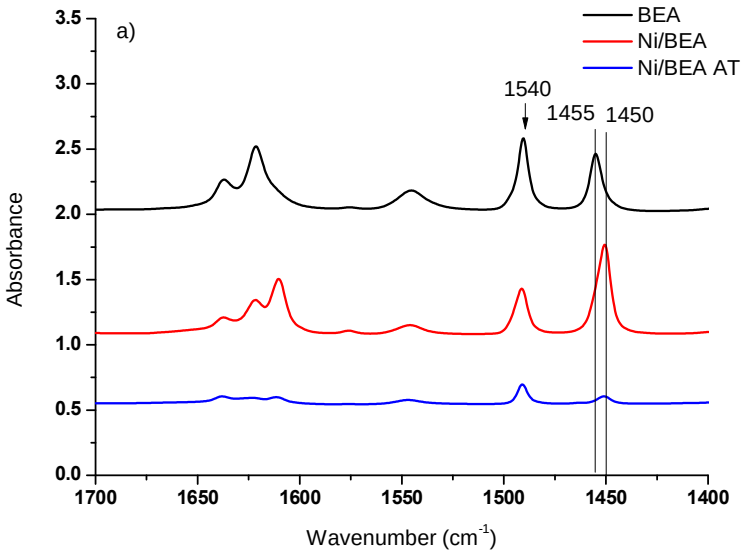

642

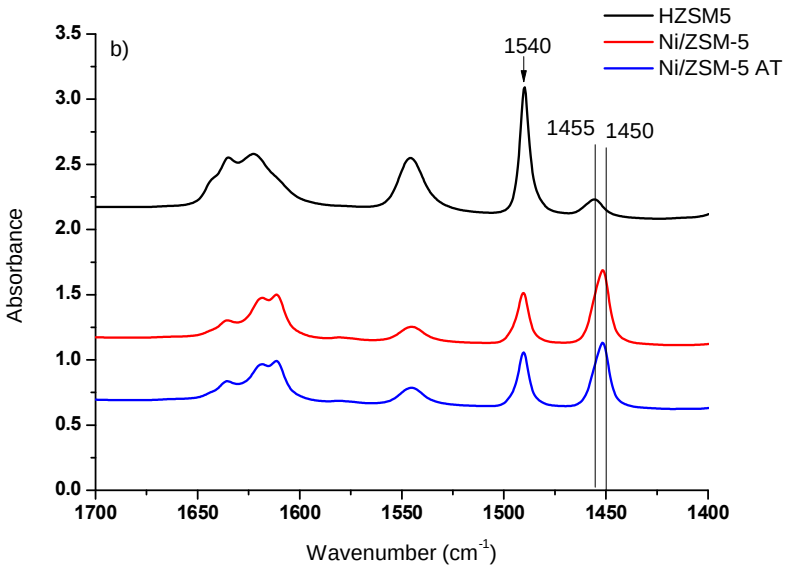

643 **Figure 5** ï FTIR spectra observed after the adsorption of pyridine on zeolite based catalysts: a
644 BEA; b ZSM-5

645

646

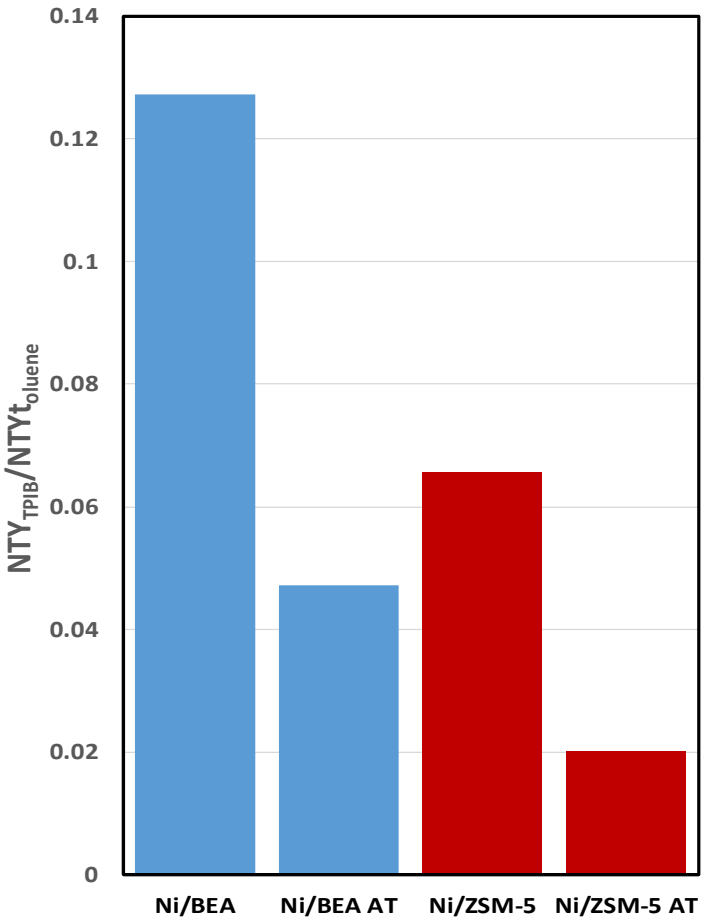

Figure 6 -Ratio of NTY_{TIPB} to $NTY_{toluene}$ for Ni/BEA and Ni/ZSM-5 zeolites before and after extraction.